Journal of Materials Chemistry A

Accepted Manuscript

ROYAL SOCIETY OF CHEMISTRY

www.rsc.org/materialsA

Journal Name

ARTICLE

Heading towards Novel Superior Silicon-based Lithium-ion Batteries: Ultrasmall Nanoclusters Top-down Dispersed over Synthetic Graphite Flakes as Binary Hybrid Anodes

Received 00th January 20xx,
Accepted 00th January 20xx

DOI: 10.1039/x0xx00000x

www.rsc.org/

Yao-Hui Huang[a], Chih-Tse Chang[a], Qi Bao[a], Jenq-Gong Duh[a,*], Yu-Lun Chueh[a].

A prominent anodic material of silicon ultranano particles (SiUPs, size < 10 nm) using recycled Si wafer fractures as raw materials and further improvement called top-down dispersion for high-capacitive Li-ion batteries has been addressed originally in this work. Economic benefits and outstanding electrochemical properties, including shorter Li-ion diffusive paths and low-strained effects as a result of the unique ultra-nanometric structure, enable such SiUPs to possess superior advantages for scalable manufacturing procedures as compared to other nanometric Si powders and become the priority of starting materials for Si-based anodes potentially. Meanwhile, an advanced top-down dispersive process has been optimized systematically to prevent severe particles aggregations to ameliorate the electrochemical performance of SiUPs electrodes. In addition to avoiding pre-aggregations, this top-down dispersion brings in adequate buffer spaces, constructed by dispersive media (graphite flakes) and well-dispersive ultrasmall SiUPs nanoclusters (size < 100 nm), alleviating drastic volume variation and local stress during cycling. These improved SiUPs electrodes maintained 1200 mAh g^{-1} sepcific capacity over 300 cycles under a high current density of 0.8 A g^{-1}, coupled with ca. 98.5% reversibility. On the basis of these advantages, including low cost, facile manufacture and high performance, this original method provides a pathway to achieve commercial high-capacitive Si-C composite anodes for Li-ion batteries.

Introduction

For meeting the requirements of transportation electrification and renewable energy integration,[1-3] silicon (Si) has been considered one of most promising next-generation anodic materials for developing lithium ion batteries (LIBs) with a high energy and power density because of its high theoretical gravimetric capacity (~3579 mAh g^{-1} for $Li_{15}Si_4$ at room temperature), operational safety, abundant availability and environmental benignity.[4-6] Despite these notable advantages, a large volume change (> 300 %) that occurs during the insertion and extraction processes of Li^+ always results in the severe pulverization of active Si materials and the loss of electrical contact with conductive additives and current collectors. In particular, at high current densities for charging and discharging, the inferior capacitive fading is inevitable.[7-9] For mitigating this intrinsic drawback, several strategically advantageous architecture designs have been proposed including: (i) compositing with conductive carbonaceous materials, such as carbon nanotubes (CNTs) and graphene, to maintain the electrical contact of the electrodes during volume change;[10-15] (ii) surface modification to increase its Coulombic efficiency (CE) and cycling retention by releasing the interfacial reaction to achieve a more stable and compact solid–electrolyte interface (SEI) formation on the surface of active materials;[16-18] (iii) constructing a buffer space for active materials—such as solid frameworks, core-shell, and yolk-shell structures—to alleviate the drastic volume expansion;[14,19-23] and (iv) dimensional morphological control through particular fabrications to obtain nano- to microscale materials, such as 0D nanoparticles (SiNPs), 1D nanowires/nanotubes, 2D nanopaper and 3D porous particles, to accommodate the large strain variation, reduce the solid-state diffusion length, and increase the surface area contact with electrolytes, thereby benefiting the high rate charge/electron transfer.[4,8,24-29] For decades, numerous remarkable cycling performances have been achieved and reported in highlights of those excellent modifications.

Although some studies have obtained favorable results for Si-based anodes with such state-of-the-art modifications, their methods still face critical challenges that should be overcome before their industrialization and commercialization. For example, the high expense but low yield of Si sources derived mainly from chemical vapor deposition (CVD) involving organic precursors,[30,31] the chemical reduction of silica-containing materials by using Mg powders,[32-34] and noble metal-assisted etching with metallurgical Si,[35,36] greatly limit the competitiveness with commercial graphite. Nevertheless, scalable recyclable Si nanoparticles (SiNPs) powders from the slicing waste of Si slug or organosilane industrial processes may prospective candidates for further fabricating Si-based anodes because of their distinguishing source economy and sustainability. However, their extrinsic properties such as nonuniform size distribution and severe particle aggregation require further

[a] Department of Materials Science and Engineering, National Tsing Hua University, Taiwan.
*, Prof. J. -G. Duh (E-mail: jgd@mx.nthu.tw)

improvement to achieve acceptable electrochemical performance of LIBs.[37,38] Moreover, some intricate and costly processes, such as extremely harsh reactive conditions (high temperature, anti-atmosphere), multitasking, time consumption, energy overuse, expensive reactants and low productivity (noble metals, CVD), also hinder their pathways towards industrialization. Therefore, for developing extensive original sources and modification methods, the yield and cost concerns should not be ignored and must be assigned priority to realize the commercialization of Si-based anodes in the future.

This paper demonstrated a top-down dispersion manufacturing process for fabricating well-dispersed ultrasmall Si nanoclusters (size < 100 nm) within a graphite-constructed 3D matrix for next-generation high capacity anodes in LIBs. For this original and industry-directed process, several critical aforementioned limitations were considered to achieve a practical and high capacity anode. First, an industrial manufacturing process of anodic etching under well-controlled conditions has been introduced to prepare porous Si wafers fractures composed of numerous holey channel networks at an ultrananо scale (< 10 nm).[24,39-41] In-situ powderized ball milling for groundbreaking fabrication of SiUPs for large-scale production was developed using the recycled Si wafer fractures from solid waste in the solar cell industry as an alternatives to LIBs.[42] Furthermore, for the purpose of achieving strain-free active structures by creating buffer spaces,[14,19-23] a breakthrough yet facile dispersion process, called top-down dispersion, was addressed originally in this study as demonstrated in Figure 1. Without any inert gas- or liquid-phase protective support, this top-down dispersion, originated from in-situ powderized ball milling was used to etch the Si fragments with conductive/dispersive media (graphite flakes, KS6), delivered an immediate manufacturing method that yields high performance active anodic composites productively, instead of seriously agglomerated Si powders.

Experimental Section

Active Materials Synthesis

The large-scale production of porous Si with ultrananо frameworks has been carried out primarily through electrochemical anodized etching the cutting waste fractures of p-type Si wafers from photovoltaic cells manufacturing industries.[24,39-41] The overall experimental schematic was illustrated in Figure A.1. Firstly, the as-received waste fractures of Si wafer were fixed on a customized etching cell. They were kept in close contact with a Ti plate used as the anode while a Pt electrode was used as the cathode. Hydrofluoric acid and dehydrated alcohol with the volume ratio of unity was mixed and prepared for the etching solution. Then, the waste wafer fractures were etched under a current density of 100 mA cm^{-2} for 30 minutes and the porous Si layers with ultrananо frameworks were created with the etched thickness more than 250 μm. The uniform detachment of etched porous layer from the substrate was achieved after another three time higher current densities etching (350, 425 and 500 mA cm^{-2}). During the operating process, the Ti electrode should be prevented from damage by the etching solution. The etched Si fragments were washed by deionized water and ethanol repetitively to remove the remanent etching solution.

Afterwards, the so-called top-down dispersion process was conducted using as-etched porous Si fractures and graphitic flakes (KS6, ALDRICH) as the starting materials. The etched-Si fractures were introduced along with the dispersive media with the mass ratio of 3 : 1 (denoted as TD-SiUPs-31), into a zirconium-oxide type ball-milling vial. The mass ratio of zirconium-oxide balls-to-specimen was 4 : 1. The TD-SiUPs-31 composite powder was obtained on a planetary ball mill at 200 rpm for 2 h and the milling yield (defined by the mass ratio of specimen after and before the ball milling process) was higher than 90%. All fabrication processes were carried out under the atmospheric condition in accordance with potential industrialization. Moreover, samples in different Si/KS6 weight ratio of 1 : 1 and 2 : 3, which were denoted as TD-SiUPs-11 and TD-SiUPs-23, were prepared as well. Furthermore, sole SiUPs without graphitic flakes were fabricated by ball-milling the etched-Si fractures. For comparison, the control sample (m-SiUPs) was fabricated directly by ball-milling the as-prepared SiUPs powders rather than the etched Si fractures and dispersive media following the mass ratio of 3 : 1. In other words, this control sample was prepared via ball-milling processes but with different starting

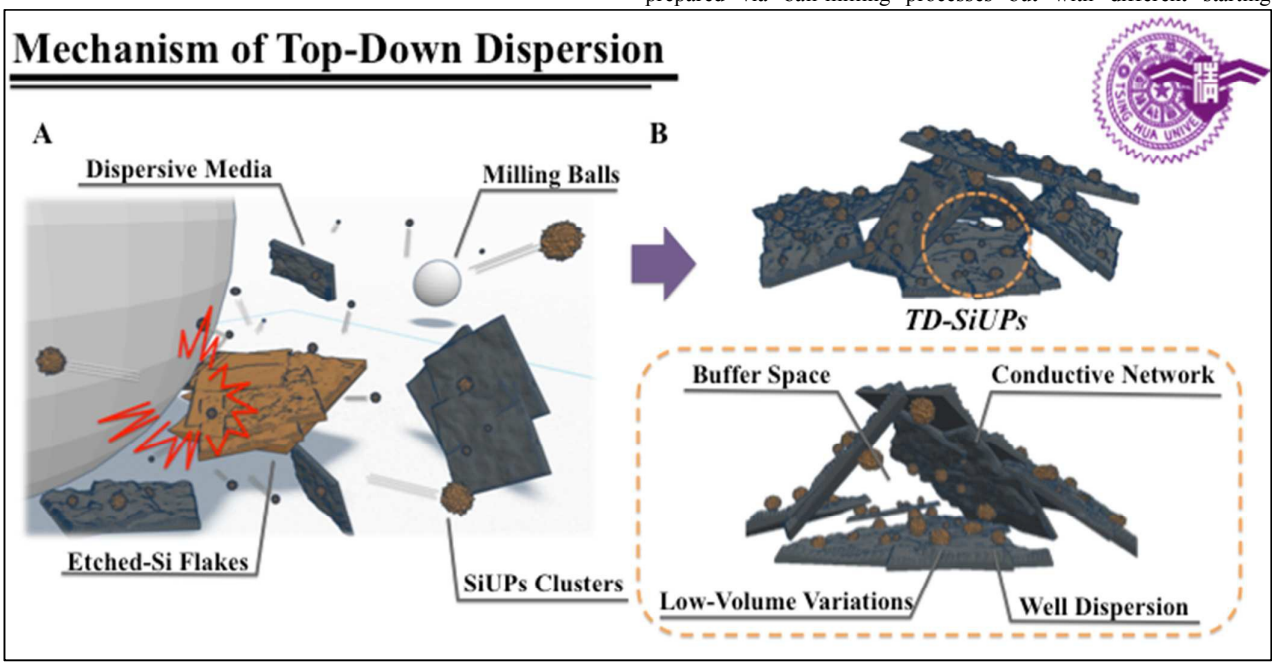

Figure 1. Schematic illustrations of (A) Mechanism of Top-down dispersive processes (B) TD-SiUPs and its advanced features.

materials to exclude the simultaneous in-situ powderization and top-down dispersion process. These comparative experiments highlighted the positive effect of the in-situ powderization and top-down dispersion on the electrochemical properties.

Materials Characterization

The phases and crystal patterns of as-prepared composites were characterized by X-ray diffraction (XRD) (TTRAX III, RIGAKU, Japan) and high-resolution transmission electron microscopy (HR-TEM, JEOL Cs Corrected Field Emission TEM, Japan). X-ray photoelectron spectroscopy (XPS, ULVAC-PHI PHI 5000 Versaprobe II) was conducted to investigate the surface elemental information and approximate component characterization of SiUPs. Morphological assessments of cycled electrodes were performed on a field emission scanning electron microscopy (FE-SEM, JEOL 7600F, Japan). Brunauer–Emmett–Teller (BET) surface analysis was investigated by N_2 adsorption-desorption isotherms, which were collected at 77 K using physisorption analyzer (ASAP 2020, Micromeritics, USA).

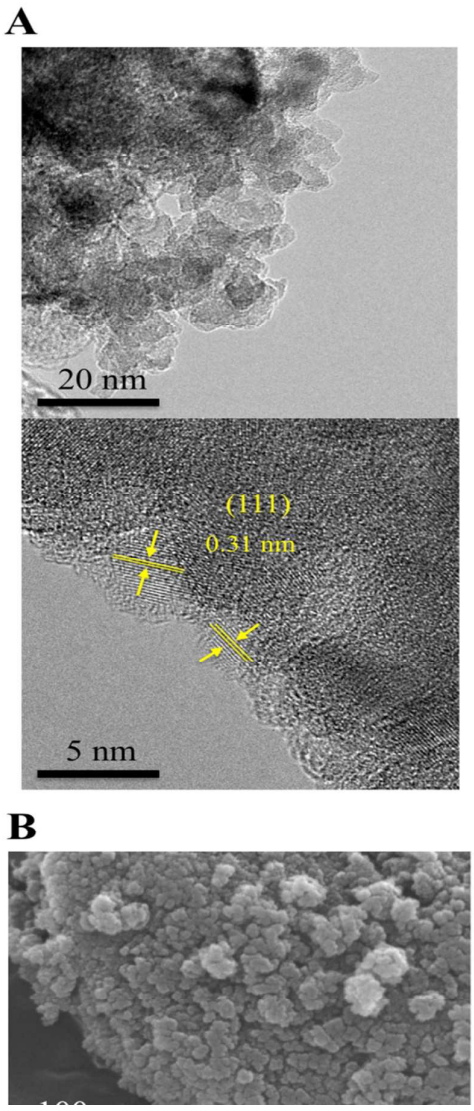

Figure 5-1. (A) The HR-TEM images of as-prepared SiUPs (B) The FE-SEM image of as-prepared SiUPs.

Electrodes Fabrication and Materials Synthesis

The composites composed of SiUPs and dispersive media via different manufacturing processes were studied as active materials. In all cases, the working electrodes were prepared by casting slurry containing of active materials (80 wt%), carboxymethyl cellulose (CMC) binders (15 wt%) and conductive carbon black (Super P, 5 wt%) on a piece of copper foil. The active mass loading was about 1.6 mg/cm^2. All the electrodes were dried for 12 h at 135 °C under vacuum. The electrochemical properties were evaluated on CR2032 coin half-cells with Li foil as the counter/reference electrode. The electrolyte for all tests was LiPF6 (1M) dissolved in a mixture of ethylene carbonate (EC) and diethyl carbonate (DEC) (1:1 in volume, Samsung Co.). The cells were assembled in an argon-filled glove box (O2 < 0.1ppm. H2O < 0.1ppm) and cycled by galvanostatical charging/discharging between 0.01 and 1.2 V versus Li^+/Li on a multichannel testing system (Arbin, BT2000, USA) under the certain current density of the mass corresponding to active materials. The cyclic voltammetry tests were performed on an electrochemical workstation (Ametek 263A, USA) at a scan rate of 0.1 mV s^{-1}.

Results & Discussion

Characteristic and Electrochemical Investigations of Ultranano Silicon Particles

Size-dependent issues for the raw materials of Si as LIBs anode have been widely discussed to ameliorate the cycling performance. According to pioneering reports, beddings of cracks and fractures during lithiation/delithiation could be avoided intrinsically for Si particles with the critical size less than ~150 nm.[8,22,43,44] Moreover, except for avoiding the intrinsic cracking on Si particle during cycling, the stability of formed SEI and diffusive path of lithium ion within Si particles were also taken into highly considerations to achieve the optimal cycling performance. The world-leading LIBs research group revealed that the optimal size of Si was about ~15 nm to achieve the compromised cycling performance.[45] Referring to these theories, acceptable cyclability will be met through reducing the size of Si particles less than 15 nm. Hence, in this study, a scalable approach was addressed originally to acquire Si particles in ultranano size (SiUPs, < 10 nm) as the priority of Si for LIBs anode in next decades. The experimental processes in detail are illustrated as schematic diagram in Figure A.1. After facile manufacturing processes, morphological characterizations of SiUPs obtained from waste etched-Si fragments are revealed in Figure 2. As revealed in Figure 2A, according to the high-resolution transmission electron microscopy (HR-TEM) analysis, the size of the single crystalline particle of SiUPs was less than 10 nm correlated to etched-Si frameworks as shown in Figures A.1B and A.1C before in-situ powderized ball-milling with an interlayer spacing of 0.317 nm of (111) plane. The SiOx amorphous layer with the thickness less than 3 nm formed on the surface of SiUPs were observed in the HR-TEM images. It is worth noting that the presence of Si-O amorphous layer attributed by intense phase interaction between SiUPs and atmosphere act as apposite interface for transferring Li^+ ions and alleviating the volume variation.[46-49] Additionally, after the Platinum deposition with the thickness of about 5nm, authentic investigations of morphology and nanostructure under the ultranano scale for SiUPs was available from FE-SEM images in Figure 2B.

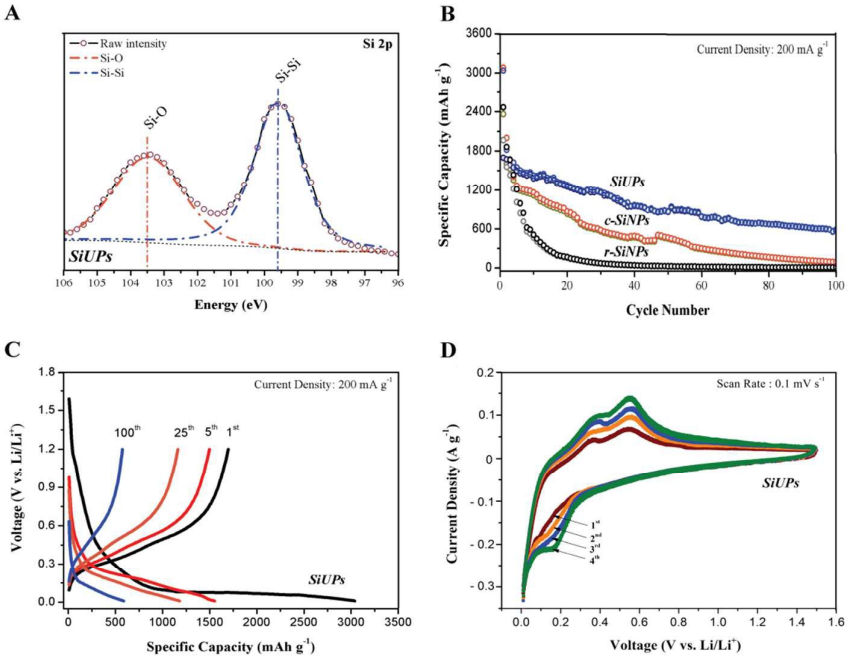

Figure 3. (A) Si 2p XPS of as-prepared SiUPs. (B) Cycling capacity for 100 galvanostatic cycles of SiUPs, c-SiNPs and r-SiUPs. The rate was 0.1 A g^{-1} for the first three cycle and 0.2 A g^{-1} for following cycles. (C) Voltage profiles of different galvanostatic cycles of the SiUPs.(D) Cyclic voltammogram of SiUPs between 1.5 V and 0.01 V versus Li/Li^+ at scan rate of 0.1 mV s^{-1} for first 4 cycles.

X-ray Photoelectron Spectroscopy (XPS) supports more comprehensive information about surface characterization of SiUPs. Full scanning spectra (Figure A.2A) identifies that the presence of Si (Si 2p, peaks located at ~100 eV and Si 2s, peaks located at ~150 eV), and oxygen (O 1s, peaks located at ~530 eV) from SiUPs powder.[47,48] High-resolution scanning spectra of Si 2p core-level XPS, as revealed in Figure 3A, indicates two types of Si bonding, i.e., Si-Si (Si 2p, the peak at 99.7 eV), and Si-O (Si 2p-O, the peak at 103.5 eV), which ascribed to represent various energy states. Since that the measured depth using XPS (≤ 10 nm) is theoretically in accordance with the overall size of single SiUPs, the summation areas below Si-Si and Si-O peaks give the additional instructions to estimate the relative quantitative of two kinds of bonds approximately. The fraction of Si-O in overall detected Si-related signals was 0.358 as an estimation of the content of SiO_x within single SiUPs. On the basis of above observations, the intrinsic size in ultranano scale and the existence of SiO_x outer layer lead to the most superior electrochemical performance as raw materials of Si compared with other two raw materials, i.e. the recycled Si powder (r-Si) from waste of sliced Si slug and commercial Si powder (c-Si) via chemical synthesis (Optical and FE-SEM images were illustrated in Figure A.3). Figure 3B and 3C depict exceptional property of SiUPs with the high-quality retained capacity of 602.3 mAh g^{-1} after 100 cycles at a cycling rate of 200 mA g^{-1}. The charge/discharge behaviors were all in accordance with the typical SiNPs sources characterized by cyclic voltammograms (CV) tests accompanied with the Li^+ intercalation voltage of ~0.2 V and deintercalation voltages of ~0.34 and ~0.56 V. Comparative information of intrinsic characteristics for three specimens is summarized in Table A.1. Although structural collapse and capacitive fading induced by massive local expansion during cycling do require further improvements, however, it is undeniable that SiUPs may be the one of befitting raw materials in Si-based LIBs.

Achieving Superior Binary Anode through A Top-down Dispersion Process

For general physical mixing course initiated from active powders, insufficiency of mixing energy and agitators with large volume related to active particles is one of primary limitations to disperse particles below nanoscale homogenously, which cause the local aggregation and capacitive fading in Si-based anode. In literatures, state-of-the-arts architectural controls of active materials in Si-based anode have been considered as most practical modifications to achieve the outstanding cycling performance.[4,5,10-23] Herein, an originally dispersive method, called "top-down dispersion", to pursue a facile and effective manufacturing process accompanied with this scalable fabrication of SiUPs is proposed in this study. The core solution of top-down dispersion was relied on the premix of fragile etched-Si fragments and dispersive media following in-situ powderized ball-milling as shown in Figures 1 to deliver a breakthrough dispersive process, and this specimen prepared by top-down dispersion was denoted as TD-SiUPs-31. The reason for selecting carbon materials in the shapes of flakes as dispersive media was to obtain architectural constructions for achieving expansion-relived 3D frameworks and conductive network. As compared to this original dispersive process, a general mixing process with the initial materials, SiUPs powder and dispersive media, were also conducted to prepare the comparisons represented as m-SiUPs. The schematic diagram depicting the primary difference of dispersive situations is illustrated in Figure 4A. XRD analysis was used to investigate the crystal phases of the as-prepared samples, as shown in Figure 4B. Three diffraction peaks at a value of 2θ at 26.5°, 44.5°, and 54.6°corresponded to the (002), (100), and (101) planes of the hexagonal carbon material (JCPDS, No. 41-1487), respectively. Other diffraction peaks at a value of 2θ at 28.4, 47.3, and 56.0 which can be assigned to the (111), (220), (311), (331), and (422) planes of crystalline silicon (JCPDS, No. 27-1402), exhibited relatively strong diffraction intensity.

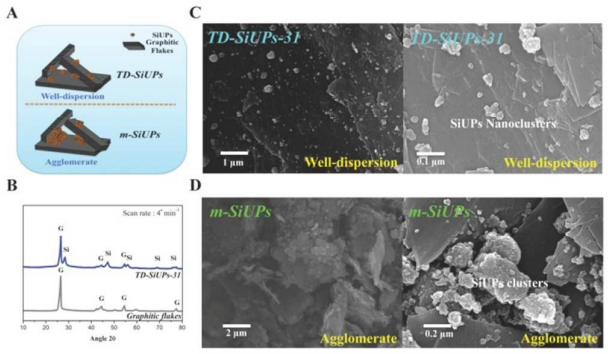

Figure 4. (A) The schematic illustration of TD-SiUPs-31 and m-SiUPs. (B) XRD patterns of TD-SiUPs and KS6 at a scan rate of 4° min^{-1}. (C) and (D) FE-SEM images of TD-SiUPs-31 and m-SiUPs.

The Top-down dispersion process reveals several crucial ameliorations, including: i) direct in-situ powderization from fragile Si segments avoid the pre-aggregation of SiUPs and lead to reduced size of SiUPs nanoclusters to increase the reacted area with electrolyte, ii) SiUPs nanoclusters dispersed by conductive media homogeneously prevent the structural disruptions from drastic local expansion during cycling, and iii) extra buffer spaces and robust 3D conductive networks constructed by graphite flakes conductors strengthen the overall working electrode to endure the volume variation. FE-SEM images demonstrated in Figures 4C and 4D would determine the effect of top-down dispersion process straightly. Manufacturing via top-down dispersion process, SiUPs nanoclusters in TD-SiUPs-31 (Figure 4C) with the size smaller than 100 nm were decorated on dispersive media instead of serious particle aggregation. However, m-SiUPs (Figure 4D) showed severe agglomerations of primary SiUPs clusters beyond the size of 200 nm gathered in regional space, which may bring about the drastic local expansion and structural disruptions irreversibly. Furthermore, High-resolution TEM images and low-magnification SEM images were provided in Figures A.4 and A.5 to show the overall features of fabricated composites. Another characterization to determine the difference of dispersive situations was revealed by BET analysis in Figure A.6. An obvious hysteresis phenomenon for m-SiUPs indicated that excessive inner nano-spaces inside SiUPs agglomerates hindered the desorptive behaviors of absorbed nitrogen gas on inner surface.[50,51]

Deriving from above advanced architectural designs for mitigating structural disruptions, superior cycling performance was achieved with this innovative manufacturing process as promising anodes in LIBs. It is notable to point out that all reported capacities

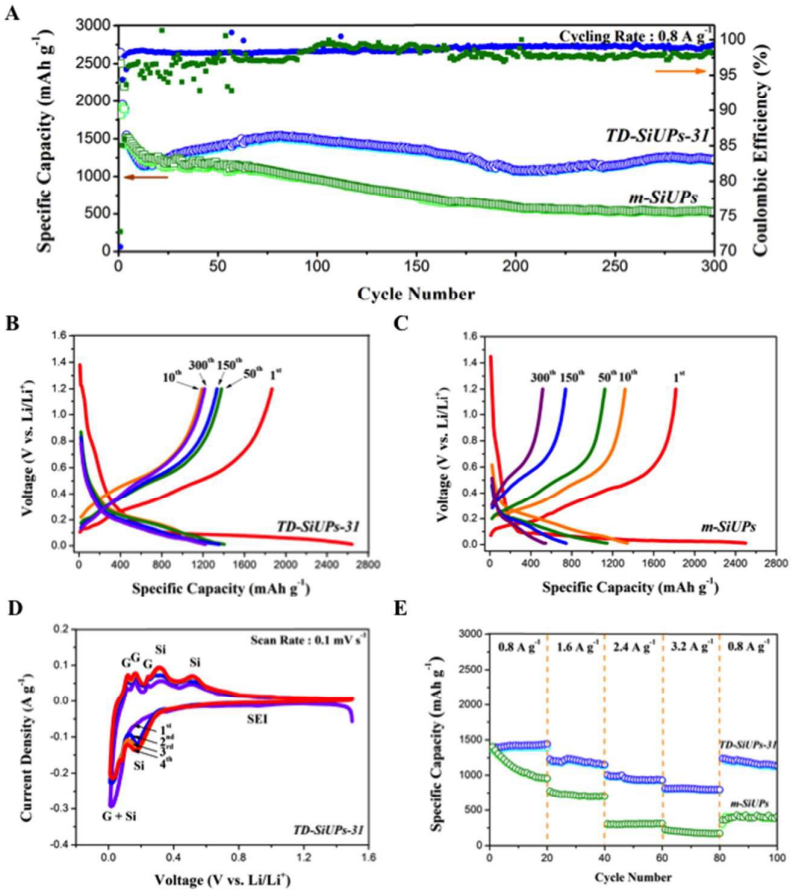

Figure 5.(A) Galvanostatic cycling capacity and Coulombic efficiencies of TD-SiUPs-31 and m-SiUPs. The current rate was 0.2 A g^{-1} for the first three cycles and 0.8 A g^{-1} for the following cycles. (B), (C) Voltage profiles of the different cycles corresponding to (A) for the TD-SiUPs-31 and m-SiUPs. (D) Cyclic voltammogram of TD-SiUPs-31 between 1.5 V and 0.01 V versus Li/Li^+ at scan rate of 0.1 mV s^{-1} for the first four cycles. (E) Rate performance of TD-SiUPs-31 and m-SiUPs at various charging current ranged from 0.8 A g^{-1} to 3.2 A g^{-1}.

were calculated on the basis of the total weight of active materials including SiUPs (~75%) and graphite flakes. Upon galvanostatic cycling between 0.01 and 1.2V, pre-activation were conducted at a low current rate of 200 mA g^{-1} for the first three cycles and the following cycles were carried on at a high current rate of 800 mA g^{-1}. Figure 5A shows the cycling performances of TD-SiUPs-31 and m-SiUPs cells for 300 cycles. The capacitive fading during the first 20 cycles might be derived from the drastic volume expansion caused by particle aggregation, leading to the slight irreversible damage of the original conductive network. The gradual increase in capacity during the first dozens of cycles indicated an activation process for the TD-SiUPs-31 electrode. This could be explained by the increase of reactive area to the electrolyte for the small SiUPs nanoclusters to achieve fully reactive state after several times of structural variation during the cycling process. Similar activation processes were also observed in those state-of-the-art architectural designs with outstanding electrochemical performances.[4,5,19-23,28] After such activation process, the TD-SiUPs-31 cell reached its highest discharge reversible capacity of 1502.5 mAh g^{-1} and then maintained almost stable without obvious capacity decay. The excellent cycling performance of TD-SiUPs-31 was probably contributed by the strain-alleviated structure originated from the ultrasmall SiUPs nanoclusters well-dispersed within the 3D buffering space built by the conductive framework of graphite flakes. The outstanding electrochemical stability rendered the TD-SiUPs-31 to accomplish a long-term (300 cycles) cycling test with impressive capacity retention of 80.56% (1210.4 mAh g^{-1}) at a high current density of 800 mA g^{-1}. The average Coulombic efficiency (CE) of the cells for 300 cycles is 98.64%, indicating an excellent reversibility, which is inclined to the industrial feasibility. Generally, the relative low CE in the first cycle (70.21%) was caused by the formation of solid/electrolyte-interface (SEI) layer on the surface of SiUPs and their dispersive media, graphitic flakes, as result of their high surface area as shown in Figure 4D. As a comparison, the m-SiUPs cells exhibit an inferior cycling performance with only 280.6 mAh g^{-1} of discharge capacity has retained after 300 cycles, corresponding to the capacitive retention of 36.47% of its highest discharged capacity (769.2 mAh g^{-1} at a current density of 800 mA g^{-1}). The primary cause of capacitive fading in the m-SiUPs anodes for the long-term cycling test is their structural deterioration from drastic volume expansion. Additionally, this defective structural design brought in a disturbed deviation of CE, averaged a relative low value of 97.32% for 300 cycles. Moreover, the electrochemical properties of sole dispersive media are shown in Figure A.7 as supporting information.

The according voltage profiles of the TD-SiUPs-31 and m-SiUPs of their 1st, 10th, 50th, 150th and 300th cycles between 0.01 and 1.2 V at a current density of 800 mA g^{-1} are shown in Figures 5B and 5C. All charging/discharging curves performed by Si/Graphite composites matched well with reported literature. In the first cycle, both specimens exhibited a typical charging (lithiation) platform of silicon at ~0.1 V. Co-dominated by both SiUPs and graphite flakes, the lithiation process in the first cycle curve showed a slight protrusion from 0.8V to 0.4V, which might be caused by the gradual formation of stable SEI.[52,53] In the following cycles, this typical charging platform gradually disappeared as most literature reported, showing a highly correlation with the further discussions on the electrochemical behaviors of TD-SiUPs-31 examined by cyclic voltammograms (CV) as shown in Figure 5D. In the first cathodic scan, the branch between 0.5 to 1.2V was attributed to the intensive interface reaction between the active materials and the electrolyte, leading to the formation of SEI layer. The appearance of a peak around 0.1V indicates that Li ions intercalated into graphitic layers and alloyed with Si, coupled with a phase transition from crystalline

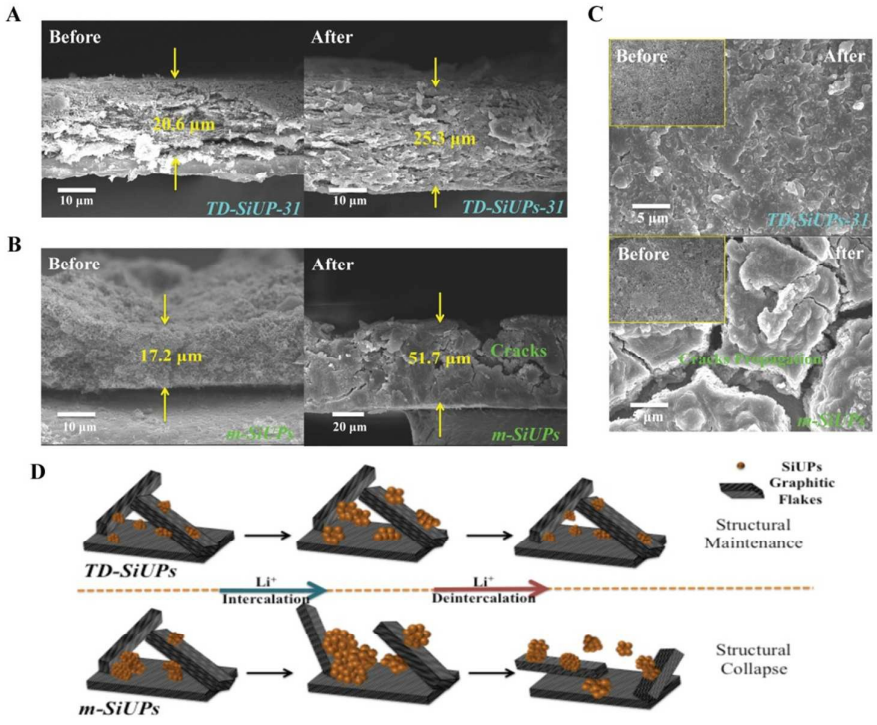

Figure 6. (A), (B) Cross-sectional FE-SEM images of electrode of TD-SiUPs-31 and m-SiUPs before and after 300 galvanostatic cycling test at a current density of 0.8 A g^{-1} (C) FE-SEM images of the surface of TD-SiUPs-31 and m-SiUPs electrodes before and after cycling. The inset images are the surface of electrodes before cycling. (D) The schematic illustration of hypothesis of alleviated mechanisms for TD-SiUPs and m-SiUPs.

phase (Si) to the amorphous phase (Li_xSi). When the potential scan reversed, four apparent peaks are identified, which could be related to the deintercalation of LiC_6 and the delithiation of Li_xSi, respectively. The deintercalations of Li^+ out of graphite flakes corresponded to the peaks around 0.22 and 0.27 V.[54] The other two peaks at 0.34 and 0.51 V were ascribed to the delithiation process of Li_xSi to Si phase. During the following cycles, the additional cathodic peak current at 0.18 V and the anodic peak currents around 0.34 and 0.51V increased gradually.[4-15] The rate performances of TD-SiUPs-31 and m-SiUPs at a series of increased current densities of 0.8, 1.6, 2.4, and 3.2 A g^{-1} are compared in Figure 5E. The TD-SiUPs-31 cells exhibited superior rate performance and reached high capacities of 987.2, and 765.4 mAh g^{-1} at the high current densities of 2.4 and 3.2 A g^{-1}, respectively. However, based on the above-mentioned hypothesis about the drastic local expansion from agglomerated SiUPs clusters, the m-SiUPs electrodes were unable to withstand fast charging and discharging processes, resulting in a low capacity of 208.3 mAh g^{-1} at the high current density of 3.2 A g^{-1}.

For anode materials with high capacity, the volume change and structural variation propagating to the macroscopic scale of whole electrodes have highly correlations to fading cycling performances due to the collapse of conductive networks. In other words, the direct observation for the integrity of the cycled electrodes would be another support to indicate the outstanding long cycling performance. In this work, all achievements are obtained from the cycled electrodes after 300 cycles at a current rate of 800 mA g^{-1}, and fully delithiated state. As revealed in Figure 6B, excessive cracks emerged and propagated over the surface of m-SiUPs electrodes induced by the local strain on the entire electrode during the charged/discharged progress (inset). In contrast, a reduction in the spread of cracks at the presence of TD-SiUPs-31, as shown in Figure 6C, gave the evidence of the large-scaled alleviation on the local strain by the well-dispersed Si nanoclusters within the buffer space built by graphite flakes. Another indication to determine the degree of volume variation was revealed by the cross-sectional FE-SEM images of the cycled electrodes. An obvious increase in the thickness of the cycled TD-SiUPs-31 and m-SiUPs electrodes is shown in Figures 6B and 6C. The slighter change in the thickness (122.81%) demonstrated the strain-relief effects of the TD-SiUPs-31 electrode, as compared to that of m-SiUPs (298.84%). Thus, based on the above comprehensive electrochemical and morphological analysis, it is reasonable to predict the possible strain-alleviation mechanism in microscope, as illustrated in Figure 6D, which rooted in reducing active particles size into ultranano scale and scattering SiUPs nanoclusters homogeneously through a top-down dispersion process. Such a structural-destruction-proof architecture helped effectively to release the local strain within its buffering space.

Acting as one of the critical factors on elevating the electrochemical performance, the dispersive media in TD-SiUPs, which provide the conductive network and expansive buffer space, was highly emphasized on following discussions. Informative and systematic confirmations were further conducted on the effect of dispersive media with different contents by electrochemical means. Two specimens were prepared via the top-down dispersion method with different initial weight ratios of SiUPs to KS6, 1 : 1 and 2 : 3, as denoted as TD-SiUPs-11 and TD-SiUPs-23. The above-mentioned TD-SiUPs-31 with relative low content of KS6 (25%) was also compared together. It is revealed in Figure 7A that TD-SiUPs-11 and TD-SiUPs-23 exhibited the discharge capacity of 1083.6 mAh g^{-1} and 898.7 mAh g^{-1} after 200 cycles, respectively. Information of

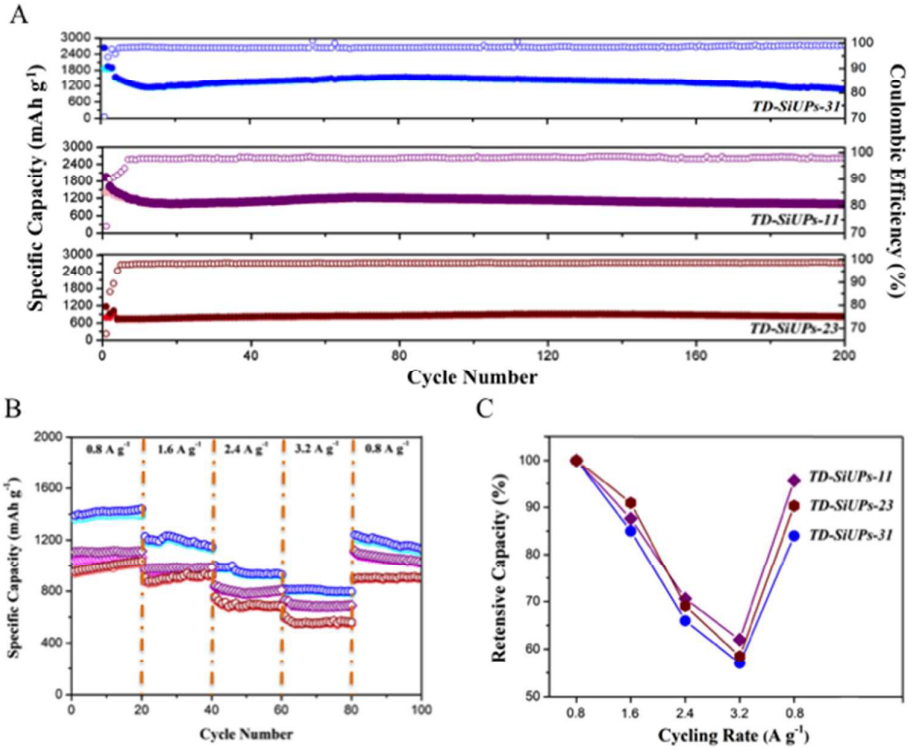

Figure 7. (A) Cycling performance and Coulombic efficiencies for different weight ratio of SiUPs and dispersive media for 3 : 1, 1 : 1, and 2 : 3, which were denoted as TD-SiUPs-31, TD-SiUPs-11, and TD-SiUPs-23. All cycling tests were conducted at current rate of 0.2 A g^{-1} for the first three cycles and 0.8 A g^{-1} for the following cycles. (B) Rate performances for TD-SiUPs-31, TD-SiUPs-11, and TD-SiUPs-23 at various charging current ranged from 0.8 A g^{-1} to 3.2 A g^{-1}. (C) The relationship of reversible capacity ratio and corresponded current densities.

Coulombic efficiency performed by TD-SiUPs-11 and SiUPs-23 were revealed in Figure A.8. The measured Coulombic efficiencies of both electrodes were over 98%. As the increase amount of dispersive media scattered the SiUPs nanoclusters, more buffering space and solid conductive network was made, then more stable cycling performances was obtained. Furthermore, detailed analysis of rate performances is also summarized in Figures 7B and 7C. Higher capacity was retained for specimen composed of more dispersive media, which might result from the fact that large quantity of intricate conductive networks promoted the electrochemical reaction between the electrolyte and SiUPs nanoclusters at higher cycling rates. After rapid charge/discharge examinations, larger than 5.1% of discharge capacity over that of TD-SiUPs-31 is retained for TD-SiUPs-11 and TD-SiUPs-23 electrodes since that more fabricated buffer spaces and continuous conductive networks enable to accommodate the intrinsic expansion from SiUPs nanoclusters. Based on the above comprehensive discussion, the dispersive media have been recognized to play a role as the structural stabilizer and the electrical connector in this original system processed by the so-called top-down dispersion.

Conclusions

In conclusion, SiUPs smaller than 10 nm were successfully fabricated via facile and scalable processes, including anodic etching and general ball-milling from the waste of solar-cell industry as the superior starting materials in high-performance Si-based Li-ion battery negative electrode. Depending on advantages of ultra-nano-sized effects, which provide added interfaces and paths for transferring electrons and ions rapidly, as well as firmly strained variation during cycling, SiUPs exhibited overwhelming cycling performance compared to other practical raw materials of Si powder, such as nanometric powders and recycled sliced powders. Furthermore, unique top-down dispersive processes were introduced originally as an extensive modification on SiUPs to achieve outstanding electrochemical cycling performance. This method addressed a facile dispersive process without liquid-based support for preventing local expansions induced from severe particles aggregations, which lead to capacitive fading from disconnections between SiUPs and conductive materials. In contrast to electrodes prepared by traditional physical-mixing methods, with their improved performance, top-down dispersion electrodes are capable of achieving over 300 cycles and retaining high reversible capacity more than 1200 mAh g^{-1} at a current rate of 0.8 A g^{-1} without significant capacity decay. In addition, the described top-down dispersive processes may be extended to other raw materials with fragile properties that experience large-volume changes and unstable SEI formation during cycling. Therefore, according to the above-described competitive advantages, industrialization will follow up these innovative manufacturing procedures and realize requirements of low-cost and high-performance battery to be eligible for commercial high-energy Li-ion batteries.

Acknowledgements

This work was financially supported from the Ministry of Science and Technology of Taiwan (Grant Nos. MOST 104-2622-E-007-001-CC1). The authors thank to Chin-Kai Lan for XRD, FESEM measurements and, Ying-Mei Chang and Cheng-Yu Wu for HR-TEM measurements at the National Tsing Hua University.

Notes and references

1 M. Armand, and J. M. Tarascon, Nature, 2008, **451**, 652.
2 P. G. Bruce, B. Scrosati, and J. M. Tarascon, Angew. Chem. Int. Ed., 2008, **47**, 2930.
3 O. K. Park, Y. Cho, S. Lee, H. C. Yoo, H. K. Song, and J. Cho, Energy Environ. Sci., 2011, **4**, 1621.
4 H. Wu, and Y. Cui, Nano Today, 2012, **7**, 414.
5 M. T. McDowell, S. W. Lee, W. D. Nix, and Y. Cui, Adv. Mater., 2013, **25**, 4966.
6 J. Deng, H. Ji, C. Yan, J. Zhang, W. Si, S. Baunack, S. Oswald, Y. Mei, and O. G. Schmidt, Angew. Chem. Int. Ed., 2013, **52**, 2326.
7 M. E. Stournara, X. Xiao, Y. Qi, P. Johari, P. Lu, B. W. Sheldon, H. Gao and V. B. Shenoy, Nano Lett., 2013, **13**, 4759.
8 X. H. Liu, L. Zhong, S. Huang, S. X. Mao, T. Zhu, and J. Y. Huang, ACS Nano, 2012, **6**, 1522.
9 S. W. Lee, M. T. McDowell, L. A. Berla, W. D. Nix, and Y. Cui, Proc. Natl. Acad. Sci. USA, 2012, **109**, 4080.
10 X. Zhou, Y. Yin, L. Wan, and Y. Guo, Adv. Energy Mater., 2012, **2**, 1086.
11 W. J. Lee, T. H. Hwang, J. O. Hwang, H. W. Kim, J. Lim, H. Y. Jeong, J. Shim, T. H. Han, J. Y. Kim, J. W. Choi, and S. O. Kim, Energy Environ. Sci., 2014, **7**, 621.
12 Q. Xiao, Y. Fan, X. Wang, R. A. Susantyoko and Q. Zhang, Energy Environ. Sci., 2014, **7**, 655.
13 X. Wang, G. Li, F. M. Hassan, M. Li, K. Feng, X. Xiao, and Z. Chen, J. Mater. Chem. A, 2015, **3**, 3962.
14 Y. Huang, Q. Bao, B. Chen, and J. Duh, Small, 2015, **11**, 2314.
15 N. Lin, J. Zhou, Y. Zhu, and Y. Qian, J. Mater. Chem. A, 2014, **2**, 12604.
16 F. M. Hassan, V. Chabot, A. R. Elsayed, X. Xiao, and Z. Chen, Nano Lett., 2014, **14**, 277.
17 X. Xiao, P. Lu, and D. Ahn, Adv. Mater., 2011, **23**, 3911
18 H. T. Nguyen, M. R. Zamfir, L. D. Duong, Y. H. Lee, P. Bondavalli and D. Pribat, J. Mater. Chem. A, 2012, **22**, 24618.
19 N. Liu, Z. Lu, J. Zhao, M. T. McDowell, H. Lee, W. Zhao, and Y. Cui, Nat. Nanotechnol., 2014, **9**, 187.
20 H. Wu, G. Yu, Li. Pan, N. Liu, M. T. McDowell, Z. Bao, and Y. Cui, Nat. Commun., 2013, **4**, 1943.
21 S. Li, X. Qin, H. Zhang, J. Wu, Y. He, B. Li, and F. Kang, Electrochem. Commun., 2014, **49**, 98.
22 N. Liu, H. Wu, M. T. McDowell, Y. Yao, C. Wang, Y. Cui, Nano Lett., 2012, **12**, 3315.
23 H. Wu, G. Zhang, N. Liu, T. J. Carney, Y. Yang, and Y. Cui, Nano Lett., 2012, **12**, 904.
24 M. Ge, J. Rong, X. Fang, and C. Chou, Nano Lett., 2012, **12**, 2318.
25 A. M. Chockla, J. T. Harris, V. A. Akhavan, T. D. Bogart, V. C. Holmberg, C. Steinhagen, C. B. Mullins, K. J. Stevenson and B. A. Korgel, J. Am. Chem. Soc., 2011, **133**, 20914.
26 M. Park, M. G. KIM, J. Joo, K. Kim, J. Kim, S. Ahn, Y. Cui, J. Cho, Nano Lett., 2009, **9**, 3844.
27 J. Li, C. Yue, Y. Yu, Y. Chui, J. Yin, Z. Wu, C. Wang, Y. Zang, W. Lin, J. Li, S. Wu and Q. Wu, J. Mater. Chem. A, 2013, **1**, 14344.
28 Z. Zhang, Y. Wang, W. Ren, Q. Tan, Y. Chen, H. Li, Z. Zhong, and F. Su, Angew. Chem. Int. Ed., 2014, **53**, 5165.
29 M. R. Zamfir, H. T. Nguyen, E. Moyen, Y. H. Lee, and D. Pribat, J. Mater. Chem. A, 2013, **1**, 9566.
30 A. Esmanski, and G. A. Ozin, Adv. Funct. Mater., 2009, **19**, 1999.
31 A. Magasinski, P. Dixon, B. Hertzberg, A. Kvit, J. Ayala, and G. Yushin, Nat. Mater., 2010, **9**, 353.
32 N. A. Liu, K. F. Huo, M. T. McDowell, J. Zhao, and Y. Cui, Sci. Rep., 2013, **3**, 1919.
33 D. S. Jung, M. H. Ryou, Y. J. Sung, S. B. Park, and J. W. Choi, Proc. Natl. Acad. Sci. USA, 2013, **110**, 12229.
34 F. Du, B. Li, Y. Xiong, K. Wang, and J. Chen, Adv. Mater., 2014, **26**, 6145.

35 D. Y. Chen, X. Mei, G. Ji, M. H. Lu, J. P. Xie, J. M. Lu, and J. Y. Lee, Angew. Chem., 2012, **124**, 2459.
36 S. Yoo, J. Lee, S. Ko, and S. Park, Nano Energy, 2013, **2**, 1271.
37 J. Yu, H. Zhan, Y. Wang, Z. Zhang, H. Chen, H. Li, Z. Zhong, and F. Su, J. Power Sources, 2013, **228**, 112.
38 L. Shi, W. Wang, K. Yuan, and Y. Yang, J. Mater. Chem. A, 2014, **2**, 20213.
39 J. H. Park, L. Gu, G. Maltzahn, E. Ruoslahti, S. N. Bhatia, and M. J. Sailor, Nat. Mater., 2009, **8**, 331.
40 K. Kusová, O. Cibulka, K. Dohnalova,I. Pelant, J. Valenta, A. Fucıkova, K. Zıdek, J. Lang, J. Englich, P. Matejka, P. Stepanek, and S. Bakardjieva, ACS Nano, 2010, **4**, 4495.
41 L. Moretti, G. Abbate, A. Marino, L. Rotiroti, I. Rea, I. Rendina, and L. De Stefano, Opt. Express, 2006, **14**, 6264.
42 L. Russo, F. Colangelo, R. Cioffi, I. Rea, and L. D. Stefano, Materials, 2011, **4**, 1023.
43 X. H. Liu, and J. Y. Huang, Energy Environ. Sci., 2011, **4**, 3844.
44 Y. Oumellal, N. Delpuech, D. Mazouzi, N. Dripré, J. Gaubicher, P. Moreau, P. Soudan, B. Lestriez, and D. Guyomard, J. Mater. Chem., 2011, **21**, 6201.
45 R. Yi, F. Dai, M. L. Gordin, H. Sohn, and D. Wang, Adv. Energy Mater., 2013, **3**, 1507.
46 Y. Hu, R. Demir-Cakan, M. Titirici, J. Müller, R. Schlögl, M. Antonietti, and J. Maier, Angew. Chem. Int. Ed., 2008, **47**, 1645.
47 T. Morita, and N. Takami, J. Electrochem. Soc., 2006, **153**, A425.
48 F. Dai, R. Yi, M. L. Gordin, S. Chen, and D. Wang, RSC Adv., 2012, **2**, 12710.
49 J. C. Guo, A. Sun, and C. S. Wang, Electrochem. Commun., 2010, **12**, 981.
50 D. S. Kim, J. Jeon, and K. Shin, Micropor. Mesopor. Mat., 2013, **181**, 61.
51 I. U. Arachchige, and S. L. Brock, J. Am. Chem. Soc., 2006, **128**, 7964.
52 N. A. Kaskhedikar, and J. Maier, Adv. Mater., **2009**, 21, 2664.
53 X. X. Wang, J. N. Wang, H. Chang, and Y. F. Zhang, Adv. Funct. Mater., 2007, **17**, 3613.
54 M. Holzapfel, H. Buqa, F. Krumeich, P. Novák, F. Petrat, and C. Veit, Electrochem. Solid-State Lett., 2005, **8**, A516.